UvA-DARE (Digital Academic Repository)

Limits on Astrophysical Antineutrinos with the KamLAND Experiment

Abe, S.; Decowski, M.P.; KamLAND Collaboration

[Link to publication](#)

Limits on Astrophysical Antineutrinos with the KamLAND Experiment

S. Abe[1], S. Asami[1], A. Gando[1], Y. Gando[1], T. Gima[1], A. Goto[1], T. Hachiya[1], K. Hata[1], S. Hayashida[1,23], K. Hosokawa[1],
K. Ichimura[1], S. Ieki[1], H. Ikeda[1], K. Inoue[1,2], K. Ishidoshiro[1], Y. Kamei[1], N. Kawada[1], Y. Kishimoto[1,2], T. Kinoshita[1],
M. Koga[1,2], N. Maemura[1], T. Mitsui[1], H. Miyake[1], K. Nakamura[1], K. Nakamura[1], R. Nakamura[1], H. Ozaki[1,3], T. Sakai[1],
H. Sambonsugi[1], I. Shimizu[1], Y. Shirahata[1], J. Shirai[1], K. Shiraishi[1], A. Suzuki[1], Y. Suzuki[1], A. Takeuchi[1], K. Tamae[1],
K. Ueshima[1,24], Y. Wada[1], H. Watanabe[1], Y. Yoshida[1], S. Obara[4], A. K. Ichikawa[5], A. Kozlov[2,25], D. Chernyak[2,26],
Y. Takemoto[6,27], S. Yoshida[6], S. Umehara[7], K. Fushimi[8], S. Hirata[9], K. Z. Nakamura[10], M. Yoshida[10], B. E. Berger[2,11],
B. K. Fujikawa[2,11], J. G. Learned[12], J. Maricic[12], S. N. Axani[13], L. A. Winslow[13], Z. Fu[13], J. Ouellet[13], Y. Efremenko[2,14],
H. J. Karwowski[15,16], D. M. Markoff[15,17], W. Tornow[2,15,18], A. Li[16], J. A. Detwiler[2,19], S. Enomoto[2,19], M. P. Decowski[2,20],
C. Grant[21], T. O'Donnell[22], and S. Dell'Oro[22]
(KamLAND Collaboration)

[1] Research Center for Neutrino Science, Tohoku University, Sendai 980-8578, Japan
[2] Institute for the Physics and Mathematics of the Universe, The University of Tokyo, Kashiwa 277-8568, Japan
[3] Graduate Program on Physics for the Universe, Tohoku University, Sendai 980-8578, Japan
[4] Frontier Research Institute for Interdisciplinary Sciences, Tohoku University, Sendai 980-8578, Japan; shuhei.obara.d4@tohoku.ac.jp
[5] Department of Physics, Tohoku University, Sendai 980-8578, Japan
[6] Research Center for Nuclear Physics (RCNP), Osaka University, Ibaraki, Osaka 567-0047, Japan
[7] Graduate School of Science, Osaka University, Toyonaka, Osaka 560-0043, Japan
[8] Graduate School of Advanced Technology and Science, Tokushima University, Tokushima 770-8506, Japan
[9] Graduate School of Integrated Arts and Sciences, Tokushima University, Tokushima 770-8502, Japan
[10] Department of Physics, Kyoto University, Kyoto 606-8502, Japan
[11] Nuclear Science Division, Lawrence Berkeley National Laboratory, Berkeley, CA 94720, USA
[12] Department of Physics and Astronomy, University of Hawaii at Manoa, Honolulu, HI 96822, USA
[13] Massachusetts Institute of Technology, Cambridge, MA 02139, USA
[14] Department of Physics and Astronomy, University of Tennessee, Knoxville, TN 37996, USA
[15] Triangle Universities Nuclear Laboratory, Durham, NC 27708, USA
[16] The University of North Carolina at Chapel Hill, Chapel Hill, NC 27599, USA
[17] North Carolina Central University, Durham, NC 27701, USA
[18] Department of Physics, Duke University, Durham, NC 27705, USA
[19] Center for Experimental Nuclear Physics and Astrophysics, University of Washington, Seattle, WA 98195, USA
[20] Nikhef and the University of Amsterdam, Science Park, Amsterdam, The Netherlands
[21] Boston University, Boston, MA 02215, USA
[22] Center for Neutrino Physics, Virginia Polytechnic Institute and State University, Blacksburg, VA 24061, USA

Abstract

We report on a search for electron antineutrinos ($\bar{\nu}_e$) from astrophysical sources in the neutrino energy range 8.3–30.8 MeV with the KamLAND detector. In an exposure of 6.72 kton-year of the liquid scintillator, we observe 18 candidate events via the inverse beta decay reaction. Although there is a large background uncertainty from neutral current atmospheric neutrino interactions, we find no significant excess over background model predictions. Assuming several supernova relic neutrino spectra, we give upper flux limits of 60–110 cm^{-2} s^{-1} (90% confidence level, CL) in the analysis range and present a model-independent flux. We also set limits on the annihilation rates for light dark matter pairs to neutrino pairs. These data improve on the upper probability limit of ^{8}B solar neutrinos converting into $\bar{\nu}_e$, $P_{\nu_e \to \bar{\nu}_e} < 3.5 \times 10^{-5}$ (90% CL) assuming an undistorted $\bar{\nu}_e$ shape. This corresponds to a solar $\bar{\nu}_e$ flux of 60 cm^{-2} s^{-1} (90% CL) in the analysis energy range.

Unified Astronomy Thesaurus concepts: Neutrino astronomy (1100); Dark matter (353); Solar neutrinos (1511); Supernova neutrinos (1666)

---

[23] Present address: Imperial College London, Department of Physics, Blackett Laboratory, London SW7 2AZ, UK.
[24] Present address: National Institutes for Quantum and Radiological Science and Technology (QST), Hyogo 679-5148, Japan.
[25] Present address: National Research Nuclear University "MEPhI" (Moscow Engineering Physics Institute), Moscow, 115409, Russia.
[26] Present address: Department of Physics and Astronomy, University of Alabama, Tuscaloosa, AL 35487, USA.
[27] Present address: Kamioka Observatory, Institute for Cosmic-Ray Research, The University of Tokyo, Hida, Gifu 506-1205, Japan.

1. Introduction

Underground liquid scintillator neutrino detectors observe geoneutrinos, solar neutrinos, and reactor neutrinos below 10 MeV energy, in addition to the atmospheric neutrino peak at $\mathcal{O}(\text{GeV})$ range. However, other astrophysical neutrino sources also exist in our universe: from supernova explosions to hypothetical dark matter annihilation neutrinos. The valley of the neutrino energy spectrum between the end of reactor neutrinos and the onset of atmospheric neutrinos can be used to search for astrophysical neutrinos. We present a search for astrophysical neutrinos in the neutrino energy between 8.3 and

30.8 MeV, focusing on electron antineutrinos ($\bar{\nu}_e$) from the Sun, past supernovae, and dark matter annihilation.

The Sun is the dominant source of astrophysical neutrinos, and various neutrino detectors have observed solar electron neutrinos (ν_e) (Abe et al. 2011; Aharmim et al. 2013; Abe et al. 2016; Agostini et al. 2020). As discussed in Malaney et al. (1990), antineutrinos are also produced in the Sun in comparatively small amounts from beta decays of ^{40}K, ^{232}Th, and ^{238}U, and they have not been observed yet. Solar neutrinos can be converted to antineutrinos with combined processes of the Mikheyev–Smirnov–Wolfenstein (MSW) effect (Smirnov 2005) and resonant spin flavor precession (RSFP; Akhmedov 1988; Lim & Marciano 1988) as discussed in Akhmedov & Pulido (2003) and Díaz et al. (2009). This happens in a two-step process:

$$\nu_e \overset{\text{MSW}}{\rightarrow} \nu_\mu \overset{\text{RSFP}}{\rightarrow} \bar{\nu}_e, \tag{1}$$

$$\nu_e \overset{\text{RSFP}}{\rightarrow} \bar{\nu}_\mu \overset{\text{MSW}}{\rightarrow} \bar{\nu}_e. \tag{2}$$

The RSFP is a neutrino helicity resonance transition similar to the MSW effect in the Sun via the neutrino magnetic moment (μ). A simple RSFP model is excluded owing to the large neutrino magnetic moment required, $\mu > 10^{-10} \mu_{\text{B}}$, already excluded by experiments (Beda et al. 2013; Agostini et al. 2017). The μ_{B} is the Bohr magneton. The combined RSFP +MSW model is still allowed. The conversion probability is expressed as

$$P(\nu_e \rightarrow \bar{\nu}_e) \simeq 1.8 \times 10^{-10} \sin^2 2\theta_{12}$$
$$\times \left[\frac{\mu}{10^{-12}\mu_{\text{B}}} \frac{B_T(0.05R_\odot)}{10 \text{ kG}} \right]^2, \tag{3}$$

where θ_{12} is the neutrino mixing angle in the Pontecorvo–Maki–Nakagawa–Sakata matrix, B_T is the transverse solar magnetic field in the region of neutrino production, $R_\odot$ is the solar radius, and μ is the neutrino magnetic moment. Experimentally, the conversion probability for solar ^{8}B neutrinos was studied by KamLAND (Gando et al. 2012), Borexino (Agostini et al. 2021), and Super-K (Abe et al. 2020).

A supernova explosion is one of the largest neutrino burst events in our universe. Supernova neutrinos from SN 1987A, which occurred on 1987 February 23 in the Large Magellanic Cloud, were detected by the water Cerenkov detectors, KamiokaNDE (Hirata et al. 1987, 1988) and IMB (Bionta et al. 1987; Bratton et al. 1988), and the Baksan scintillation detector (Alexeyev et al. 1988). A future nearby supernova explosion could reveal detailed information on the explosion mechanism. At the same time, neutrinos from all the past supernovae are still traveling in our universe. These are called supernova relic neutrinos (SRNs), and they provide the diffuse supernova neutrino flux. The SRN energy spectrum and associated detection rates have been discussed in various models (Kaplinghat et al. 2000; Horiuchi et al. 2009; Nakazato et al. 2013, 2015). The most stringent experimental $\bar{\nu}_e$ flux upper limit is given by Super-K (Abe et al. 2021a), but no significant signal observation has been made yet. KamLAND is able to perform a comparable search for $\bar{\nu}_e$ at around 10 MeV. The higher neutron tagging efficiency should give an advantage over Super-K searching at the lower-energy region.

Neutrinos can also be produced in the annihilation of dark matter particles. In case of the existence of an MeV-scale light dark matter particle, its self-annihilation process might produce neutrino pairs ($\chi\chi \rightarrow \nu\bar{\nu}$) at MeV energies. Assuming a model of MeV-scale dark matter annihilation in our Galactic halo (Palomares-Ruiz & Pascoli 2008), the $\bar{\nu}_e$ flux from dark matter self-annihilation is given by

$$\frac{d\phi}{dE_\nu} = \frac{\langle \sigma_A \boldsymbol{v} \rangle}{2} \mathcal{J}_{\text{ave}} \frac{R_{\text{sc}} \rho_0^2}{m_\chi^2} \frac{1}{3} \delta(E_\nu - m_\chi), \tag{4}$$

where m_χ is the dark matter mass, $\langle \sigma_A \boldsymbol{v} \rangle$ is the averaged self-annihilation cross section times the relative velocity of the annihilating particles, $\mathcal{J}_{\text{ave}}$ is the angular-averaged intensity over the whole Milky Way, $R_{\text{sc}} = 8.5$ kpc is the distance of the Sun to the Galactic center, and $\rho_0 = 0.3$ GeV cm^{-3} is the local dark matter density. Here, a factor $1/3$ is assumed for the branching ratio to the three flavors of neutrinos. This process is also discussed in Klop & Ando (2018) and Argüelles et al. (2019). In this work, we show the results for two benchmark cases of $\mathcal{J}_{\text{ave}} = 1.3$ and 5.0 (Palomares-Ruiz & Pascoli 2008).

In this paper, after describing the KamLAND experiment (Section 2), we describe the search for $\bar{\nu}_e$ with an energy range of 8.3–30.8 MeV (Section 3). The main backgrounds are discussed in Section 4; these are reactor neutrinos, accidental backgrounds, spallation products, fast neutrons, and atmospheric neutrinos. The data are interpreted in Section 5, and we present the conversion probability of solar ^{8}B antineutrinos, the SRN flux, and the dark matter self-annihilation cross section. We summarize those results in Section 6.

2. KamLAND Detector

The KamLAND experiment uses an ultrapure liquid scintillator to detect $\bar{\nu}_e$ via the inverse beta decay (IBD) reaction. The detector is located 1000 m underground, underneath Mt. Ikenoyama in Kamioka Japan, corresponding to 2700 m water equivalent. The cosmic muon flux is suppressed by $\sim\mathcal{O}(10^5)$ relative to sea level. Figure 1 shows a schematic view of the detector. KamLAND consists of an 18 m diameter stainless steel sphere tank (inner detector, ID) and a cylindrical vessel of water Cerenkov muon veto (outer detector, OD) surrounding the ID. A 13 m diameter EVOH/nylon balloon (outer balloon) holds 1 kton of liquid scintillator at the center of the ID. Photon sensors, 1325 17-inch and 554 20-inch photomultiplier tubes (PMTs), sensitive to scintillation light are bolted to the inside of the stainless steel tank. Details of the detector design are described in Suzuki (2014).

KamLAND data acquisition started in 2002 March, and this study uses all data sets up to 2020 July. The KamLAND-Zen 400 phase of the project operated with a 154 cm radius nylon balloon (inner balloon) at the center of KamLAND filled with a xenon-loaded liquid scintillator from 2011 August to 2015 December (Gando et al. 2016). The detector was further upgraded in 2018 May when KamLAND-Zen 800 started with a new 1.9 m radius inner balloon (Gando 2020; Gando et al. 2021). In this study, the inner-balloon volume is vetoed to avoid possible background contamination. The OD system was refurbished in 2016, when the 225 PMTs were replaced by 140 new PMTs, including 47 higher quantum efficiency PMTs (Ozaki & Shirai 2017).

The interaction vertex and energy deposition are reconstructed using the measured PMT charge and timing information. At low energies, the detector was calibrated using various radioactive sources: ^{60}Co, ^{68}Ge, ^{203}Hg, ^{65}Zn, ^{241}Am^{9}Be, ^{137}Cs, and ^{210}Po^{13}C.
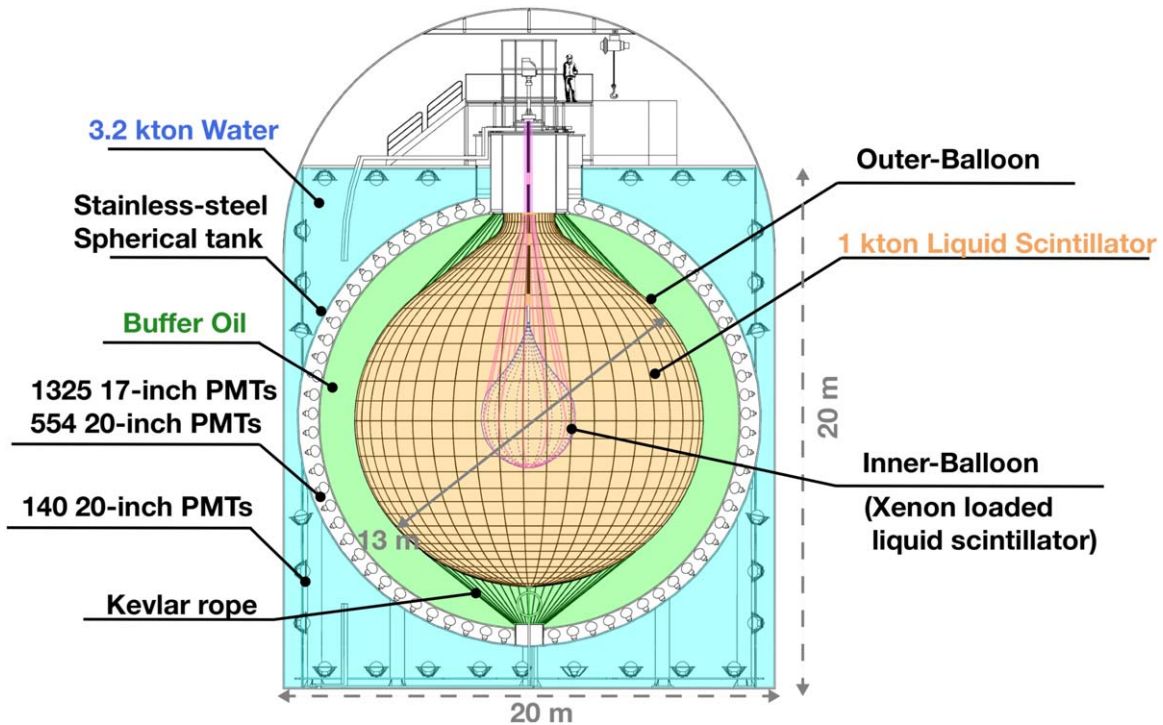
Figure 1. Schematic view of the KamLAND experiment. After the OD refurbishment campaign in 2016, the number of PMTs in the OD changed from 225 to 140 (Ozaki & Shirai 2017). The first inner balloon was installed in 2011 August.

Above 10 MeV, the energy response is calibrated using spallation products of ^{12}B ($\tau = 29.1$ ms, $Q = 13.4$ MeV) and ^{12}N ($\tau = 15.9$ ms, $Q = 17.3$ MeV).

The position-dependent energy calibration and fiducial volume determination uncertainty were studied with calibration sources positioned throughout the outer-balloon volume (Berger et al. 2009). The reconstructed energy and interaction vertex resolution were determined to be $6.4\%/\sqrt{E\,(\mathrm{MeV})}$ and $\sim 12\,\mathrm{cm}/\sqrt{E\,(\mathrm{MeV})}$ (Gando et al. 2013), respectively. Daily stability measurements were performed using 2.2 MeV gamma-rays emitted from spallation-induced neutron capture on protons (Abe et al. 2010) and spallation ^{12}B events. The total estimated uncertainty including the time variation of the energy scale, linearity, and uniformity is within $\pm 2.0\%$ for this data set.

The primary radioactive backgrounds in the liquid scintillator are $(5.0 \pm 0.2) \times 10^{-18}\,\mathrm{g\,g^{-1}}$ of ^{238}U and $(1.8 \pm 0.1) \times 10^{-17}\,\mathrm{g\,g^{-1}}$ of ^{232}Th (Gando et al. 2015). These radioactive contaminants are negligibly small relative to other backgrounds in this study, such as muon spallation products and atmospheric neutrinos, and are therefore ignored.

3. Electron Antineutrino Selection

Electron antineutrinos are detected in KamLAND via the IBD reaction ($\bar{\nu}_e + p \rightarrow e^+ + n$) with a 1.8 MeV neutrino energy threshold. IBD candidate events are selected by the delayed coincidence (DC) method: scintillation light from the positron and its annihilation gamma-rays is the prompt event, followed by a 2.2 MeV (4.9 MeV) gamma-ray from neutron capture on a proton (carbon-12) after a mean capture time of $207.5 \pm 2.8\,\mu$s (Abe et al. 2010; the delayed event). The incident neutrino energy (E_ν) is computed from the reconstructed prompt energy (E_{prompt}), $E_\nu \simeq E_{\mathrm{prompt}} + 0.8\,\mathrm{MeV} + \overline{E}_n$, where $\overline{E}_n$ is the average neutron kinetic energy of $\mathcal{O}(10\,\mathrm{keV})$.

The DC selection criteria between the prompt and delayed events use the prompt energy, delayed energy (E_{delayed}), spatial distribution (ΔR), and time difference (ΔT). They are $7.5\ \mathrm{MeV} < E_{\mathrm{prompt}} < 30\,\mathrm{MeV}$, $1.8\ \mathrm{MeV} < E_{\mathrm{delayed}} < 2.6\,\mathrm{MeV}$ or $4.4\ \mathrm{MeV} < E_{\mathrm{delayed}} < 5.6\,\mathrm{MeV}$, $\Delta R < 160$ cm, and $0.5\ \mu\mathrm{s} < \Delta T < 1000\,\mu$s, respectively. The two delayed energy selection criteria correspond to a 2.2 MeV capture gamma-ray on a proton and a 4.9 MeV capture gamma-ray on a carbon-12. The timing difference between the prompt and delayed events is required from the 207.5 μs of neutron capture time. The spatial correlation selection is optimized from diffusion length of a thermalized neutron and delayed gamma-ray. The selection efficiency is evaluated with Monte Carlo (MC) simulations described in the next paragraph. In this energy range, one of the primary backgrounds is a fast neutron (described in Section 4), mostly in close proximity to the ID vessel. In order to suppress this contamination, we select a 550 cm radius spherical fiducial volume from the center of KamLAND, corresponding to a total number of target protons of $N_p = (4.6 \pm 0.1) \times 10^{31}$.

During the KamLAND-Zen 400/800 phases, the inner-balloon regions are vetoed for the delayed event in order to avoid background contamination from the xenon-loaded liquid scintillator, inner-balloon body, and suspending ropes. The inner-balloon regions are cut from the analysis: a 250 cm radius spherical volume centered in the detector and a 250 cm radius vertical cylindrical volume in the upper half of the detector. For the above DC selection, the IBD detection efficiency ϵ_{IBD} is estimated through MC simulations with uniformly generated neutrino events and is determined to be $\epsilon_{\mathrm{IBD}} = 92\%$ (73%) without (with) the inner-balloon cut.

The data period from 2002 May to 2020 July totals 4528.5 days of live time. We find 21 DC pairs after DC selection, 3 of which have multiple delayed events following the prompt event and are excluded from the final sample, as they are likely due to
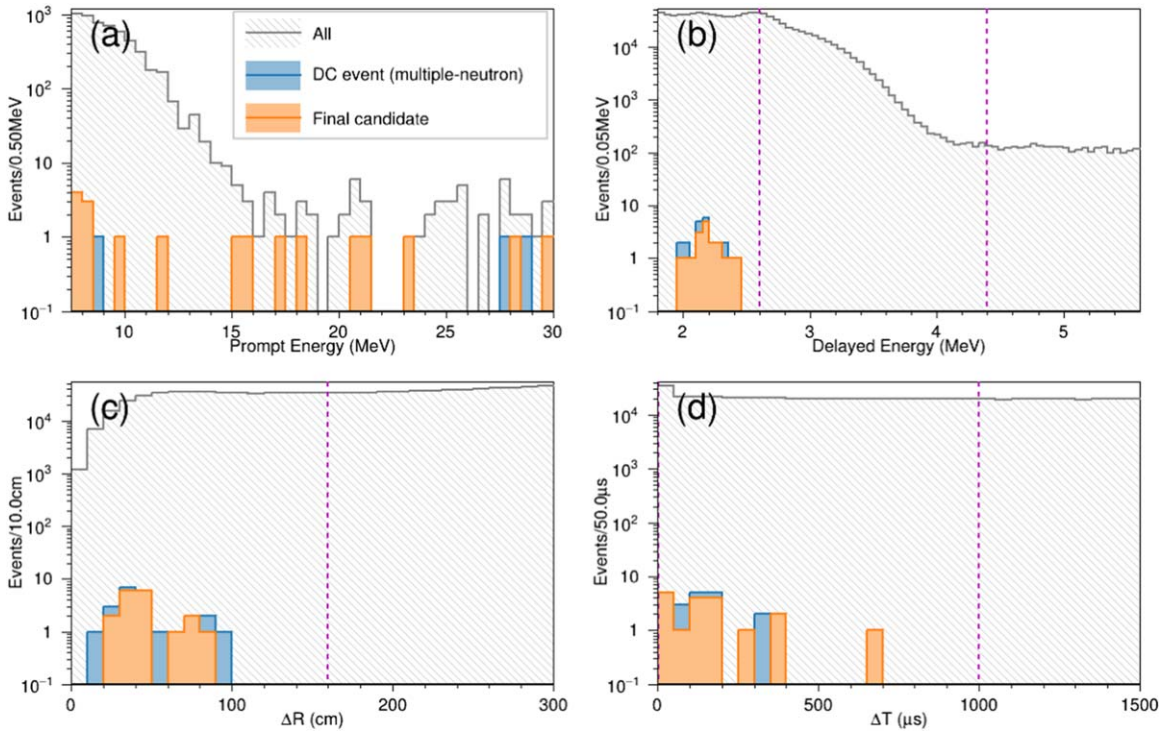
Figure 2. Event distributions for all events, after DC selection, and the final sample of 18 events: (a) prompt energy spectrum, (b) delayed energy spectrum, (c) spatial distribution between prompt and delayed events, and (d) time difference between prompt and delayed events. Vertical dashed lines correspond to cut threshold values. The blue histograms include multiple delayed neutron events and are rejected in the final candidate selection. The orange histograms are the final antineutrino candidates.

the fast neutron backgrounds and/or atmospheric neutrino interactions. Figures 2 and 3 present the electron antineutrino candidate distributions.

4. Background Estimation

Possible backgrounds in this analysis come from reactor antineutrinos, the accidental coincidence of events, spallation products, fast neutrons, and atmospheric neutrinos. Radioactive backgrounds and reactor neutrinos were studied during the reactor- and geo-neutrino measurements at KamLAND (Gando et al. 2011a, 2013), while previous $\bar{\nu}_e$ analyses in the $\mathcal{O}(10 - 10^3)$ MeV energy range (Gando et al. 2012; Asakura et al. 2015b, 2015c; Abe et al. 2021b) showed that fast neutrons and atmospheric neutrinos are the most challenging backgrounds above ∼10 MeV.

4.1. Reactor Antineutrinos

The location of the KamLAND detector is surrounded by 56 Japanese nuclear power reactors. The reactor neutrino flux comes primarily from the beta decay of neutron-rich fragments produced in the fission of four isotopes: ^{235}U, ^{238}U, ^{239}Pu, and ^{241}Pu. For each reactor, the appropriate operational records, including thermal power generation, fuel burn-up, shutdowns, and fuel reload schedule, were used to calculate the fission rates. With the reactor operation data, we have measured reactor antineutrinos between a few and several MeV (Gando et al. 2011b, 2013). However, there are no measured reactor neutrino spectra in the present analysis energy range. Hence, we use the reactor neutrino spectra assuming polynomial functions based on the results from the Institut Laue–Langevin experiment results (Huber 2011; Mueller et al. 2011). We find that the background of this analysis contribution from reactor
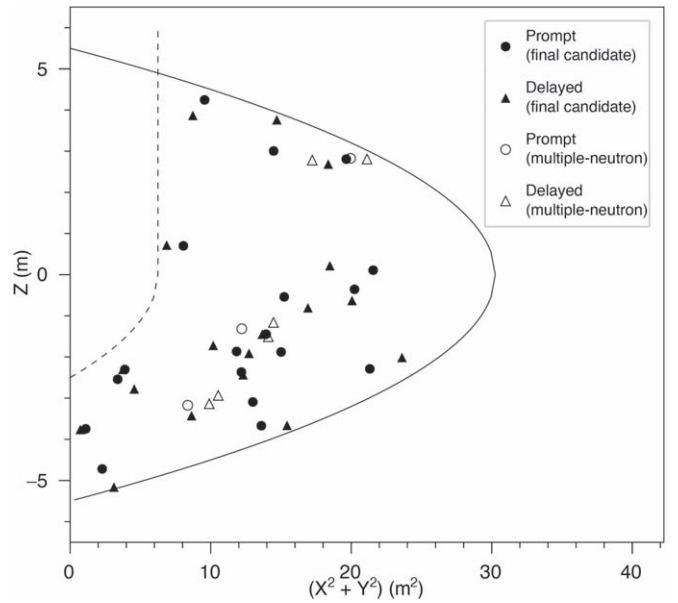
Figure 3. Position distribution after all cuts and DC selection. The filled circles and triangles are the final prompt and delayed positions, respectively. The open circles and triangles correspond to multiple-neutron DC events. The solid curve shows the fiducial radius of 550 cm, and the dashed line represents the inner-balloon cut region.

neutrinos becomes negligibly small above 10 MeV. In the range, it has a large spectrum shape uncertainty of ∼50% from the Huber/Mueller spectrum model. The number of reactor neutrino backgrounds is estimated to be 1.4 ± 0.6 including KamLAND-detector-related uncertainties. The expected number of events from the extrapolated reactor spectrum is consistent with the Daya Bay results (An et al. 2017) at

neutrino energies of [8.125, 12 MeV], the highest energy bin in the Daya Bay analysis.

4.2. Accidental Coincidence

Two uncorrelated events may accidentally pass through the DC selection. Predominantly, uncorrelated long-lived spallation isotopes or radioactive decays could produce a mimic prompt event, and radioactive decays such as ^{214}Bi and ^{208}Tl beta/gamma-rays possibly become a 2.2 MeV of mimic delayed event. To estimate the random coincidence background, events were selected with appropriate prompt and delayed energies but in an off-time window of 0.2–1.2 s after the prompt event. This off-time window is 10^3 times larger than the antineutrino selection, providing a high statistics estimate. The expected number of accidental coincidence background events is $(7.3 \pm 1.0) \times 10^{-2}$.

4.3. Spallation Products

Cosmic muons induce various spallation products in KamLAND (Abe et al. 2010). Short-lived spallation products are rejected by a 2 ms whole volume veto. Some longer-lived products are a potential background in this study. As a primary spallation cut, we apply a 2 ms whole volume veto for all muons in KamLAND, which has a muon rate of ~0.34 Hz. Muons in the ID are identified when more than $\mathcal{O}(10^4)$ photons are detected by the PMTs. We identify muon events in the OD when the number of OD hits exceeds 5 and 9, before and after the OD refurbishment campaign, respectively (Ozaki & Shirai 2017).

The previous analysis of KamLAND data (Gando et al. 2012) showed that the ^{9}Li ($\tau = 257.2$ ms, $Q = 13.6$ MeV) spallation product is a challenging background. In order to reduce this background contamination, we improved the spallation veto introducing a likelihood-ratio-based muon shower tagging in addition to the primary 2 ms veto.

Using a similar idea employed in Super-K analysis (Bays et al. 2012), we evaluate a probability density function for spallation-like events taking into consideration the spatial and timing correlation of the muon track and charge deposition. Due to low statistics of ^{9}Li in KamLAND data with a production rate of 2.8 ± 0.2 kton^{-1} day^{-1} (Abe et al. 2010), it is difficult to directly estimate the correlation between the muon track and ^{9}Li. Hence, instead of the ^{9}Li, we use ^{12}B data, whose production rate is ~20 times larger. Figure 4(a) shows the closest track distance distribution (dL) between the muon track and the spallation production point for ^{12}B, ^{9}Li, and neutrons, based on an MC study with FLUKA (version 2011.2x.8.patch; Böhlen et al. 2014; Ferrari et al. 2005) and propagated through KamLAND with GEANT4 (version 4.9.6 patch-04; Agostinelli et al. 2003; Allison et al. 2006, 2016). The spread of the ^{9}Li distance distribution is narrower than ^{12}B. This means that a tight spallation cut on the ^{12}B data can be used to put an upper limit on the remaining ^{9}Li background. The difference of muon charge deposition among the spallation products was small enough. Figure 4(b) shows the data-driven correlation between muon charge deposition per track length (dE/dX) and the distance of spallation products from the muon track (dL). Muons depositing a large charge in the detector induce spallation products even far from the muon track. Considering the lifetime of ^{9}Li, a 2 s veto is sufficient to reject the background, but the detector live time becomes too small. Here we define a likelihood-ratio parameter depending on the

dE/dX, dL, and the time difference from the muon event to the subsequent event in order to optimize the rejection of spallation events. To optimize the likelihood-ratio threshold while maximizing detector live time and minimizing the spallation cut inefficiency, we define the figure of merit (FOM) as follows (Punzi 2003):

$$\mathrm{FOM} \equiv \frac{\epsilon_{\mathrm{livetime}}}{\frac{1.64}{2} + \sqrt{N_{\mathrm{non\ spall.}} \cdot \epsilon_{\mathrm{livetime}} + N_{\mathrm{spall.}} \cdot (1 - \epsilon_{\mathrm{cut}}) + N_{\mathrm{spall.}} \cdot \sqrt{(\delta_{\mathrm{cut}}^2 + \delta_{\mathrm{stat.}}^2)}}},$$

(5)

where $\epsilon_{\mathrm{livetime}}$ is the detector live-time ratio, $N_{\mathrm{spall.}}$ ($N_{\mathrm{(non\ spall.)}}$) is the expected number of spallation (nonspallation) events without a spallation veto, ϵ_{cut} is the spallation cut efficiency depending on the likelihood-ratio threshold, δ_{cut}^2 is the cut efficiency uncertainty, and $\delta_{\mathrm{stat.}}^2$ is the statistical uncertainty on the expected number of events. Maximizing the FOM with the condition that the ^{9}Li spallation cut inefficiency becomes zero, consistent within the range determined from ^{12}B, we optimize the likelihood-ratio threshold. This muon-shower-based likelihood-ratio spallation cut allows $\epsilon_{\mathrm{livetime}} = 79\%$ of detector live time on average and gives a spallation cut inefficiency of $0.2\% \pm 0.5\%$, which means 99.8% of spallation background reduction. This gives a spallation background of 1.4 ± 3.6 in this analysis energy range.
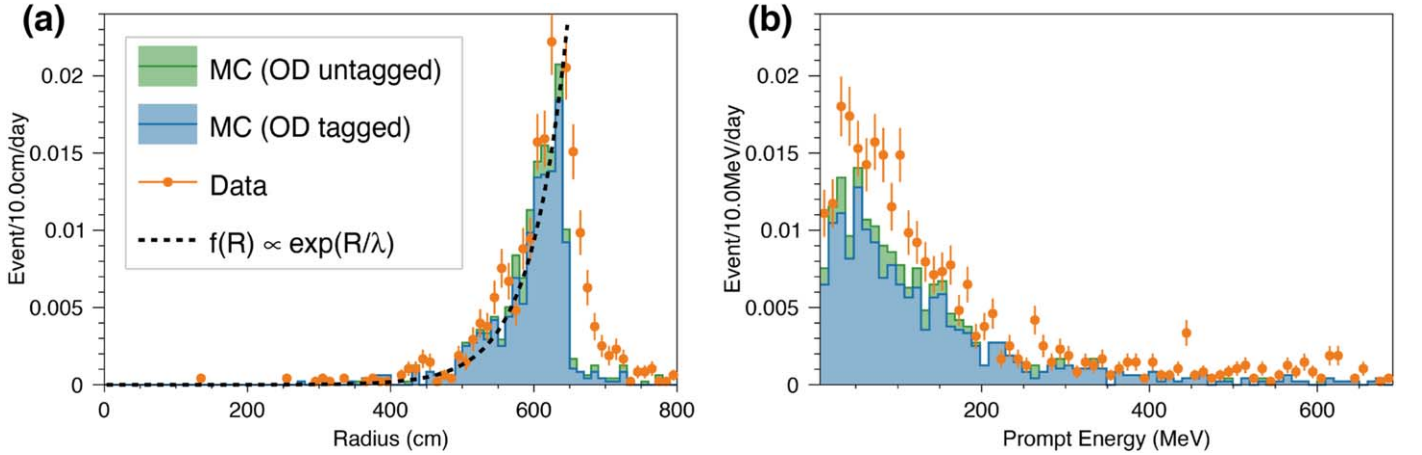
4.4. Fast Neutrons

The fast neutron background comes from outside of the detector and is induced by cosmic muons in the surrounding rock and water. Neutron scattering on protons or carbon nuclei in the liquid scintillator can mimic a prompt event. After that, the neutrons are thermalized and captured on a proton or carbon, creating the delayed event. The 2 ms veto for OD-tagged muons rejects the majority of this background, but some events remain owing to OD inefficiency.

This background was evaluated with a GEANT4-based MC, which included a detailed description of the KamLAND geometry (KLG4sim). Neutron interactions were treated with the QGSP_BIC_HP physics list, while muon–nucleus interactions were activated using G4EmExtraPhysics. The cosmic muon directional distributions were implemented from the KamLAND spallation simulation study (Abe et al. 2010), which used a topological map of Mount Ikenoyama (Geographical Survey Institute of Japan 1997) and the MUSIC simulation tool (Antonioli et al. 1997). The simulated detector response in KLG4sim was tuned with various calibration data.

An equivalent of 8313 live-time days were simulated in KLG4sim. In the case of a muon going through the ID producing a lot of scintillation emission, the muon and associated neutrons were vetoed by the 2 ms whole volume veto. Figure 5(a) shows the reconstructed fast neutron position distribution for OD-tagged MC events. For comparison, OD-tagged fast neutron events in the data are also shown in Figure 5(a). The fast neutron selection used the IBD selection described in Section 3 except for the OD tagging and $\Delta T > 10 \mu$s selection avoiding decay-electron contribution. While the data have a slightly broader spread owing to the difficulty of vertex reconstruction around the boundary between liquid scintillator and buffer oil, the radial distribution in the fiducial volume is consistent between data and simulation. The fast neutron radial distribution $f(R)$ is assumed
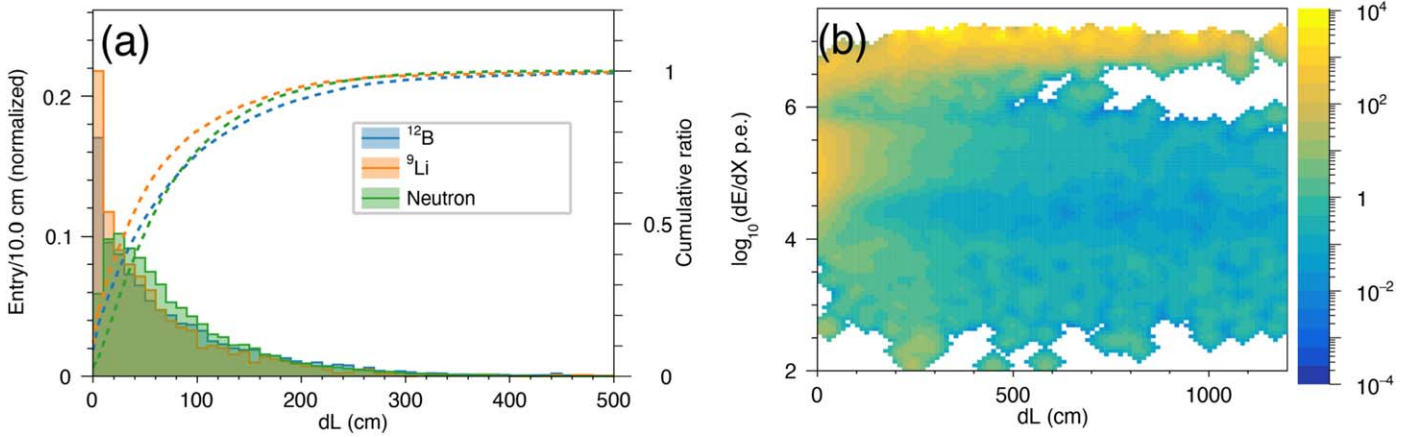
Figure 4. (a) The closest distance distribution from the muon track to the spallation products production points of ^{12}B, ^{9}Li, and neutrons from FLUKA and GEANT4 simulations. Only muons leaving more than 10^6 photoelectrons were selected in this analysis. Dashed lines correspond to the cumulative ratio (right-handed scale). 99% of these spallation products are within 300 cm from the track. (b) Data-driven correlation between muon charge deposition (dE/dX) and the closest distance of spallation product from the muon track (dL). The color bar shows the likelihood-ratio value.

Figure 5. (a) Radial distributions of fast neutron events from MC simulation in the OD-untagged case (green) and OD-tagged case (blue) in the energy range $E_{\text{prompt}} = [7.5, 30\text{ MeV}]$. The black dashed line is an exponential fit to the fast neutron distribution. (b) Energy spectra of fast neutron events within the 550 cm fiducial radius. The histograms are stacked.

to be $f(R) \propto \exp(R/\lambda)$ as a function of the distance R from the detector center, where $\lambda = 50.9 \pm 3.0$ cm. We use this nonuniform position distribution in the fit to data to evaluate the fast neutron background (see Section 5). The fast neutron energy spectra in MC and data are shown in Figure 5(b).

The remaining fast neutrons generate events with a few OD hits below the OD detection threshold, which are therefore not tagged in the OD (OD-untagged). From the KLG4sim simulation, the estimated number of fast neutron backgrounds within the fiducial volume is 6.8 ± 6.8 DC pairs by scaling the detector live time. The uncertainty is conservatively estimated to be 100%, considering the poorly known production yield of neutrons in the rock. Events producing multiple neutrons via the ^{12}C$(n, 2n)^{11}$C reaction are expected to give 3.4 ± 3.4 DC pairs.

4.5. Atmospheric Neutrinos

Atmospheric neutrinos produce the dominant background in this analysis via charged current (CC) and neutral current (NC) interactions. In the CC interactions, various neutron emission modes are possible backgrounds. Since the neutrino–nucleus interaction cross section for carbon is at least one order of magnitude smaller than for protons (Kim & Cheoun 2009), the background comes mainly from proton interactions. IBD from atmospheric electron antineutrinos is not a dominant contribution in the CC background because the mean energy is higher than our analysis energy range and small flux in this range. Based on the atmospheric neutrino flux (Honda et al. 2007) and measured cross section by MiniBooNE (Athar et al. 2007), the dominant process is $\bar{\nu}_\mu + p \rightarrow \mu^+ + n$. In the KamLAND detector, the muon decay is observed as muon scintillation, muon decay, and neutron capture. The two-prompts (muon scintillation + its decay) and one-delayed (neutron capture) DC events are vetoed with $\sim$78% efficiency (Gando et al. 2012). Its inefficiency contributes to the background. The number of CC backgrounds is estimated to be 1.1 ± 0.3.

To estimate the NC background, we took into account the atmospheric neutrino flux (Honda et al. 2007), cross sections (Ahrens et al. 1987), the neutron binding energies in carbon for the P-shell (18.7 MeV) and the S-shell (41.7 MeV) configurations and the corresponding shell populations, and de-excitation models (Kamyshkov & Kolbe 2003). The NC interaction is given by $\nu(\bar{\nu}) + {}^{12}\text{C} \rightarrow \nu(\bar{\nu}) + n + {}^{11}\text{C} + \gamma$. Most of the outgoing neutrons have a kinetic energy of less than 200 MeV, and they scatter on protons, resulting in a

Table 1
The Atmospheric Neutrino Background Study Used the Following Nuclear Interaction Models in NEUT

Interaction	Reference Model
NCQE nuclear model	Ankowski et al. (2012)
CCQE nuclear model	Gran et al. (2013)
Axial vector mass for quasi-elastic	$M_A^{QE} = 1.2$ GeV c^{-2}
Fermi momentum (NCQE)	217 MeV c^{-1}
Two-nucleon scattering (2p2h) (NC)	Not treated
(CC)	Nieves (Nieves et al. 2011)
Vector form factor (NCQE/CCQE)	BBBA05 (Bradford et al. 2006)
Axial vector form factor	Graczyk & Sobczyk (2009) and Nowak (2009)
Single pion production	Berger & Sehgal (2007)
Deep inelastic scattering	GRV98 parton distribution (Glück et al. 1998)
	with Bodek-Yang corrections (Bodek & Yang 2003)
Final state interaction	Hayato & Pickering (2021)

visible energy of typically less than 100 MeV. The details of the background signatures and estimations are described in Gando et al. (2012). The resulting expected number of NC interactions in this data set is 20.6 ± 5.9, where the uncertainty comes from the atmospheric neutrino flux and the cross section, which are combined to provide ~30% in total.

For comparison, we also estimate the atmospheric neutrino background with NEUT (version 5.4.0.1; Hayato 2009; Hayato & Pickering 2021). The interaction models are summarized in Table 1. We use the Honda et al. (2015) model for the atmospheric neutrino flux, including the matter oscillation effect implemented in Prob3++.[28] The de-excitation model for oxygen is incorporated in NEUT, but that for carbon is missing. After the final state interaction in NEUT, the outgoing particles were introduced into KLG4sim. The response of this simulation was compared to KamLAND data in the 200 MeV– 1.5 GeV energy range, outside of the fast neutron background. Although there are large uncertainties from the fast neutrons in the 30–200 MeV energy range, data and MC are consistent within the errors. Below 100 MeV, the NC quasi-elastic scattering (NCQE) is dominant. The NC two-particle-two-hole (NC 2p2h) interaction will also contribute, but assuming that the ratio of the NC 2p2h to the NCQE cross sections is similar to the corresponding CC ratio, roughly 5%–10% (Nieves et al. 2011), the contribution is estimated to be small compared to the NCQE contribution and its large uncertainties.

For the DC energy selection of 7.5–30 MeV in the NEUT-based estimation, the remaining CC and NC backgrounds are estimated to be $0.9^{+0.3}_{-0.4}$ and $16.5^{+5.1}_{-4.5}$, respectively. The NEUT background estimates are smaller but are consistent within the uncertainties. The neutron multiplicity in the NC reaction may play a role in the models and affect the background estimate owing to the DC requirement of selecting a single neutron capture. The energy spectrum shape is concrete on the de-excitation models of carbon and the proton scattering by neutrons in the numerical calculation, but this simulation-based estimation does not include the de-excitation. Therefore, we took the numerically calculated spectrum (Gando et al. 2012) and estimated the number of NC backgrounds to be 20.6 ± 5.9 in this analysis. We treat the number of NC background events as a free parameter in this analysis, independent of the number of backgrounds from the estimation models, and use the energy spectrum to constrain.

---

5. Analysis and Results

Our search for astrophysical electron antineutrino signals fitted the energy spectra and radial distributions in data to the estimated backgrounds. The fast neutron background contributes with a large uncertainty but is mostly concentrated at the outer radius, while the other backgrounds and neutrino candidates have a uniform distribution in the detector. The atmospheric neutrino NC interaction is the primary background in this analysis. We used the following χ^2 to fit the number of atmospheric NC backgrounds and the number of astrophysical neutrinos:

$$\chi^2 = \chi^2_{\text{rate}} + \chi^2_{\text{shape}} + \chi^2_{\text{penalty}} + \chi^2_{\text{BG}}, \quad (6)$$

with

$$\chi^2_{\text{rate}} = \frac{\left(N_{\text{observed}} - N_{\text{astro.}\nu} - N_{\text{NC}} - \sum_i^5 N_{\text{BG}_i}\right)^2}{\sigma^2_{\text{stat.}}}, \quad (7)$$

$$\chi^2_{\text{shape}} = \sum_n^{N_{\text{observed}}} \left\{ -2 \ln \left(\frac{\sum_j^7 N_j f_j(R) \cdot g_j(E)}{\sum_j^7 N_j} \right) \right\}, \quad (8)$$

$$\chi^2_{\text{penalty}} = \sum_k \delta_k^2, \quad (9)$$

$$\chi^2_{\text{BG}} = \sum_i^5 \frac{(N_{\text{BG}_i} - N_{\text{BG}_i}^{\text{expected}})^2}{\delta^2_{\text{BG}_i}}, \quad (10)$$

where N_{observed} is the number of observed IBD candidates, $N_{\text{astro.}\nu}$ is the number of astrophysical neutrino events, N_{NC} is the number of atmospheric neutrino NC background events, and $N_{\text{BG}_i}(i = 1, 2, \ldots 5)$ represents the number of the other background contributions (see Table 2). The statistical uncertainty $\sigma_{\text{stat.}}$ is the square root of the total number of expected events. In the shape χ^2 term (χ^2_{shape}), R is the radius, E is the energy, $f_j(R)$ is the normalized radius distribution, and $g_j(E)$ is the normalized energy spectrum for each contribution j where $j = 1, 2, \ldots, 7$ correspond to the astrophysical neutrino signal, atmospheric NC background, and the other five background contributions. We use them as an unbinned log-likelihood fit to test χ^2_{shape}. Only fast neutrons have an exponential radius distribution $f_i(R)$; the other contributions are uniform. We integrate the energy and radius over 7.5–30 MeV and 0–550 cm, respectively. The penalty term (χ^2_{penalty}) is computed from the systematic uncertainties (δ_k):

Table 2
Summary of Estimated Backgrounds and Best-fit Parameters

	Expected	Best Fit
Reactor	1.4 ± 0.6	1.3
Accidental	$(7.3 \pm 1.0) \times 10^{-2}$	7.3×10^{-2}
Fast neutron	6.8 ± 6.8	3.3
Spallation	1.4 ± 3.6	4.5
Atmospheric-ν NC	20.6 ± 5.9	7.5
Atmospheric-ν CC	1.1 ± 0.3	1.1
Solar ^{8}B $\bar{\nu}_e$	N/A	0 (best)
		5.9 (90% CL upper limit)
Total	31.4 ± 9.7	17.8 (best)
		23.7 (90% CL upper limit)
Observed	18	

energy spectrum shape uncertainty, radial distribution uncertainty, detector efficiency uncertainty, and energy scale uncertainty. In the background term (χ^2_{BG}), N_{BG_i} is the number of the ith background events, $N^{expected}_{BG_i}$ is the expected number of the ith background component, and $\delta^2_{BG_i}$ is its associated uncertainty.

5.1. Solar Electron Antineutrino

Assuming an unoscillated ^{8}B neutrino flux of $5.94 \times 10^6 \, \mathrm{cm}^{-2} \, \mathrm{s}^{-1}$ (Pena-Garay & Serenelli 2008), the region allowed by the fit is shown in Figure 6 and summarized in Table 2. The best-fit values for the $\nu_e \rightarrow \bar{\nu}_e$ conversion probability and NC events are 0.0 and 7.5 ± 3.4, respectively. The number of atmospheric neutrino NC interactions is smaller than the estimate, but model 2σ and data 2σ bands overlap. This value is also consistent with the NEUT simulation result within 1σ. Figure 7 shows the energy and radial distributions for best-fit backgrounds and the upper limit for solar ^{8}B $\bar{\nu}_e$ with 90% confidence level (CL). All residual values are within the $\pm 2\sigma$ region. The obtained upper limit on the conversion probability is 3.5×10^{-5} at 90% CL, corresponding to a $60 \, \mathrm{cm}^{-2} \, \mathrm{s}^{-1}$ solar ^{8}B $\bar{\nu}_e$ flux limit above 8.3 MeV of neutrino energy (containing 30% of the solar ^{8}B neutrino flux). In a comparable case of using a measurement ^{8}B neutrino flux of $5.25 \times 10^6 \, \mathrm{cm}^{-2} \, \mathrm{s}^{-1}$ (Aharmim et al. 2013), the upper limit on the conversion probability becomes 3.9×10^{-5} at 90% CL. This result improves on the previous KamLAND study (Gando et al. 2012) and is the most stringent upper limit to date.

From the upper limit on the conversion probability and Equation (3), we also obtain the upper limit on the neutrino magnetic moment (μ) and the transverse solar magnetic field (B_T) in the region of neutrino production:

$$\mu < 4.9 \times 10^{-10} \mu_B \left(\frac{10 \, \mathrm{kG}}{B_T(0.05 R_\odot)} \right), \qquad (11)$$

using $34°$ for the mixing angle θ_{12} (Gando et al. 2011b). This bound is weaker than the most stringent upper limit of $0.28 \times 10^{-10} \mu_B$ from the solar neutrino spectrum measurement by Borexino (Agostini et al. 2017).
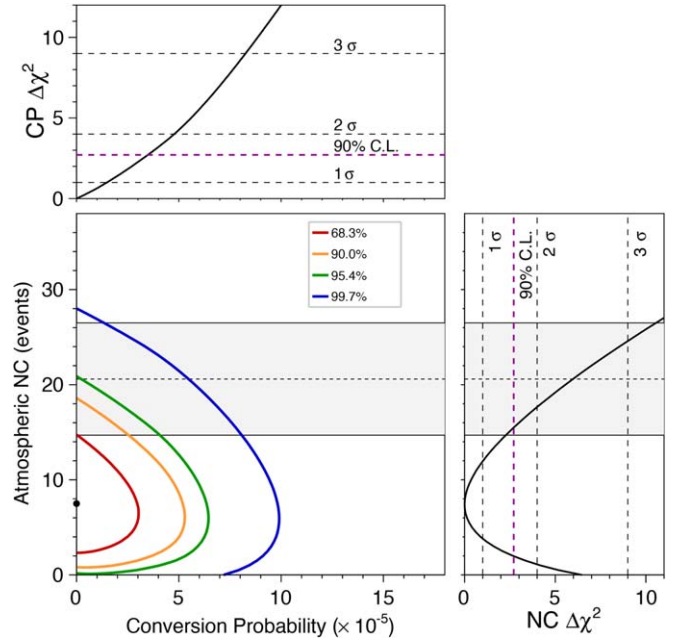

Figure 6. The results and allowed regions for the solar $\nu_e \rightarrow \bar{\nu}_e$ conversion probability and the number of atmospheric neutrino NC interactions. Color contours correspond to 1σ (red), 90% (orange), 2σ (green), and 3σ (blue). The best-fit conversion probability and NC events are 0 and 7.5, respectively (black circle). The horizontal hatched region represents the expected number of NC events with 1σ uncertainty. Top and right panels are one-dimensional $\Delta\chi^2$ distributions for conversion probability (CP) and number of atmospheric neutrino NC interactions, respectively. The upper limit on the conversion probability is 3.5×10^{-5} at 90% CL.

5.2. Supernova Relic Neutrinos

To search for SRNs, we fit with different theoretical models that produce $\bar{\nu}_e$ emission: the Kaplinghat model (Kaplinghat et al. 2000; Kaplinghat+00), the Horiuchi model in the case of 6 MeV effective temperature (Horiuchi et al. 2009; Horiuchi +09, 6 MeV), the Nakazato maximum model in the case of inverted mass ordering (Nakazato+15 max, IH), and the Nakazato minimum model in the case of normal mass ordering (Nakazato+15 min, NH; Nakazato et al. 2013, 2015). From the χ^2 defined in Equation (6), we find no significant excess of SRNs with any of the models. As an example of the fitting result with the Nakazato+15 (max, IH) model, the best-fit value for the number of SRNs is 0 events, while the number of NC backgrounds is 7.5 events. This result is consistent with the calculated number of SRN events of 0.4 in KamLAND. The 90% CL upper limit on the number of events is 9.3. The upper flux limit is calculated to be $108 \, \mathrm{cm}^{-2} \, \mathrm{s}^{-1}$ from

$$F_{90} = N_{90} \times \frac{\int_{E_{min}}^{E_{max}} \left(\frac{dF}{dE} \right)_M dE}{\int_{E_{min}}^{E_{max}} \left(\frac{dN}{dE} \right)_M dE}, \qquad (12)$$

where F_{90} and N_{90} are the upper limits on flux and the number of events, respectively. The $\left(\frac{dF}{dE} \right)_M$ and $\left(\frac{dN}{dE} \right)_M$ are the theoretical differential flux and spectrum, respectively, for the SRN models. This 90% CL flux upper limit is still much higher than the expected flux of $5.1 \, \mathrm{cm}^{-2} \, \mathrm{s}^{-1}$. Table 3 shows a
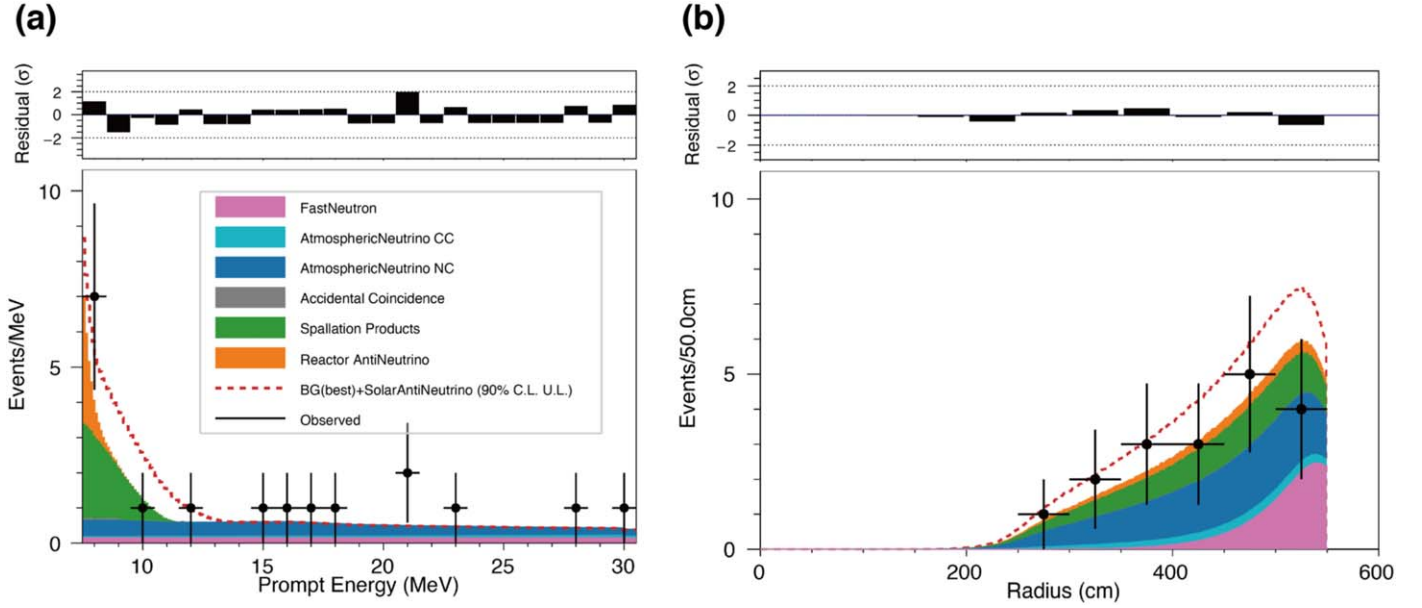
Figure 7. Results for the solar $\bar{\nu}_e$ fit for (a) the prompt energy spectrum and (b) the radial distribution. The filled histograms are the best-fit background contributions. The red dashed lines show the 90% CL upper limit for solar ^{8}B $\bar{\nu}_e$. All histograms are stacked. The top panels show residuals.

Table 3
Summary of Obtained SRN Flux and Number of Event Upper Limits (90% CL)

Model	Reference	N_{90} (Event)	F_{90} (cm^{-2} s^{-1})	Expected Flux (cm^{-2} s^{-1})
Kaplinghat+00	(Kaplinghat et al. 2000)	9.4	74.5	19.9
Horiuchi+09 (6 MeV)	(Horiuchi et al. 2009)	10.2	61.6	5.8
Nakazato+15 (max, IH)	(Nakazato et al. 2013, 2015)	9.3	108	5.1
Nakazato+15 (min, NH)	(Nakazato et al. 2013, 2015)	8.9	105	2.2

Note. F_{90} and N_{90} are the 90% CL upper limits of flux and number of events, respectively. The expected flux is integrated over our analysis energy range $E_{\rm prompt} = [7.5, 30 \text{ MeV}]$.

summary of the fit results for each theoretical model and corresponding upper limit. For all tested models, the best-fit number of SRN is 0, and NC background is 7.5. However, the reported upper limit changes for each model owing to differences in the underlying theoretical energy spectrum.

5.3. Model-independent Flux

We also present model-independent upper limits on the $\bar{\nu}_e$ flux assuming monochromatic neutrino energies. The flux upper limits (ϕ_{90}) are calculated with

$$\phi_{90} = \frac{N_{90}}{N_p \cdot \sigma \cdot \epsilon_{\rm IBD} \cdot T}, \quad (13)$$

where N_{90} is the 90% CL upper limit on the number of $\bar{\nu}_e$ in a 1 MeV wide bin using the Feldman & Cousins (1998) approach, N_p is the number of target protons, σ is the IBD reaction cross section, $\epsilon_{\rm IBD}$ is the detector efficiency, and T is the detector live time. Figure 8 shows the resulting electron antineutrino flux in comparison with results from Borexino (Agostini et al. 2021), Super-K (Bays et al. 2012; Zhang et al. 2015; Abe et al. 2021a), and various theoretical SRN models (Kaplinghat et al. 2000; Horiuchi et al. 2009;

Nakazato et al. 2013, 2015). While our results do not yet exclude SRN models, they provide the strictest flux limits for $E_\nu = [8.3, 13.3 \text{ MeV}]$. Table 4 shows a summary of the flux upper limits per bin.

5.4. Dark Matter Self-annihilation

The $\bar{\nu}_e$ flux upper limit per energy bin can be translated to a dark matter self-annihilation cross section limit (Palomares-Ruiz & Pascoli 2008). From Equation (4), we obtain an upper limit of $\langle \sigma_A v \rangle < (1{-}11) \times 10^{-24} \text{ cm}^{-3}\text{s}^{-1}$ (90% CL) for the benchmark case of $\mathcal{J}_{\rm ave} = 1.3$ (see Figure 9). This result is the most stringent constraint on the self-annihilation cross section for $m_\chi < 15 \text{ MeV}$.

6. Summary

We searched for astrophysical $\bar{\nu}_e$ in the neutrino energy range $8.3{-}30.8 \text{ MeV}$ with 4528.5 live-time days of KamLAND data. No significant excess was found over the expected backgrounds. We presented the strictest upper limit on the conversion probability of solar ^{8}B neutrinos to antineutrinos, 3.5×10^{-5} (at 90% CL). Assuming various model predictions, the upper limit on the SRN flux translates to $60{-}110 \text{ cm}^{-2} \text{ s}^{-1}$. We also give the strictest upper limit on the model-independent
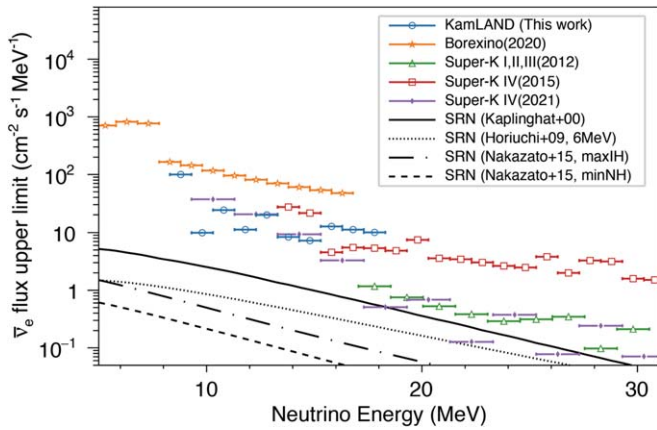
Figure 8. Model-independent upper limits on the $\bar{\nu}_e$ flux (at 90% CL). This work is compared to Borexino (Agostini et al. 2021) in the case including atmospheric neutrino background, Super-K I/II/III (Bays et al. 2012), Super-K IV (Zhang et al. 2015), and Super-K IV (Abe et al. 2021a). The black lines show different theoretical SRN fluxes.
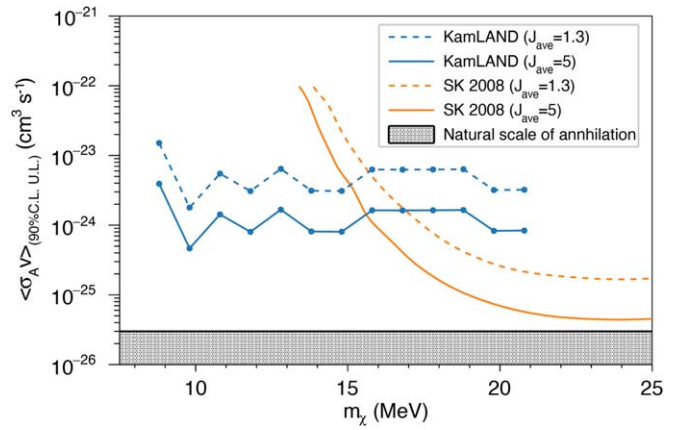

Figure 9. Upper limits on the dark matter self-annihilation cross section at 90% CL from KamLAND and Super-K (Palomares-Ruiz & Pascoli 2008). Two benchmark cases for the angular-averaged intensity $\mathcal{J}_{ave}$ are shown, $\mathcal{J}_{ave} = 1.3$ (dashed line) and 5.0 (solid line). The shadowed region corresponds to the natural scale of the annihilation cross section as 3×10^{-26} cm^3 s^{-1} (Steigman et al. 2012).

Table 4
The Obtained $\bar{\nu}_e$ Upper Flux Limit (90% CL) Assuming That All $\bar{\nu}_e$ Have a Monochromatic Energy

Energy (MeV)	Flux Upper Limit at 90% CL (cm^{-2} s^{-1} MeV^{-1})
8.3–9.3	98.1
9.3–10.3	9.5
10.3–11.3	23.8
11.3–12.3	11.2
12.3–13.3	19.8
13.3–14.3	8.4
14.3–15.3	7.3
15.3–16.3	12.8
16.3–17.3	11.2
17.3–18.3	10.1

flux below 13.3 MeV, but this limit is still an order of magnitude larger than SRN model predictions. The upper limits on the dark matter self-annihilation cross section to neutrino pairs are the most stringent for dark matter particle masses below 15 MeV. Our results for the model-independent flux limit (Table 4) can set limits on various astrophysical $\bar{\nu}_e$, for instance, neutrinos from sterile neutrino decay (Hostert & Pospelov 2021) and primordial black hole dynamics (Dasgupta et al. 2020; Calabrese et al. 2021; Wang et al. 2021).

Further background suppression is necessary to improve the solar ^{8}B $\bar{\nu}_e$ and SRN sensitivity. A future neutrino detector at a deep underground site will suppress the spallation background (Anderson et al. 2019; Guo et al. 2021). A larger distance to nuclear power plants will reduce the reactor neutrino component. More detailed measurements of the high-energy reactor neutrino spectrum are necessary, including the end point. The background arising from atmospheric neutrinos is the most challenging. Pulse shape discrimination (PSD) may reduce this contribution (Li et al. 2016) in a future large neutrino detector such as JUNO (An et al. 2016). The current KamLAND detector has the fast scintillation decay time of the liquid scintillator cocktail and significant reemission, however, PSD can be improved by the detector upgrades and by introducing excellent timing resolution for PMTs in the future. The KamLAND2 detector upgrade program intends to use a linear-alkyl-benzene-based liquid scintillator, which would realize the PSD owing to a slower scintillation decay time compared to the current KamLAND liquid scintillator (Asakura et al. 2015a; Obara et al. 2019; Nakamura et al. 2020; Kamei 2020; Takeuchi & Kawada 2020).

ORCID iDs

T. Hachiya ⓘ https://orcid.org/0000-0002-4238-7990
K. Ichimura ⓘ https://orcid.org/0000-0001-9783-5781
S. Ieki ⓘ https://orcid.org/0000-0001-7694-1921
K. Ishidoshiro ⓘ https://orcid.org/0000-0001-9271-2301
N. Kawada ⓘ https://orcid.org/0000-0003-2350-2786
J. Shirai ⓘ https://orcid.org/0000-0002-3988-2309
H. Watanabe ⓘ https://orcid.org/0000-0002-2363-5637
S. Obara ⓘ https://orcid.org/0000-0003-3488-3553
B. K. Fujikawa ⓘ https://orcid.org/0000-0002-7001-717X
A. Li ⓘ https://orcid.org/0000-0002-4844-9339
M. P. Decowski ⓘ https://orcid.org/0000-0002-1577-6229

References

Abe, S., Asami, S., Gando, A., et al. 2021b, ApJ, 909, 116
Abe, K., Bronner, C., Hayato, Y., et al. 2020, arXiv:2012.03807
Abe, K., Bronner, C., Hayato, Y., et al. 2021a, PhRvD, 104, 122002
Abe, S., Enomoto, S., Furuno, K., et al. 2010, PhRvC, 81, 025807
Abe, S., Furuno, K., Gando, A., et al. 2011, PhRvC, 84, 035804

Abe, K., Haga, Y., Hayato, Y., et al. 2016, PhRvD, 94, 052010
Agostinelli, S., Allison, J., Amako, K., et al. 2003, NIMPA, 506, 250
Agostini, M., Altenmüller, K., Appel, S., et al. 2017, PhRvD, 96, 091103
Agostini, M., Altenmüller, K., Appel, S., et al. 2020, PhRvD, 101, 062001
Agostini, M., Altenmüller, K., Appel, S., et al. 2021, APh, 125, 102509
Aharmim, B., Ahmed, S. N., Anthony, A. E., et al. 2013, PhRvC, 88, 025501
Ahrens, L. A., Aronson, S. H., Connolly, P. L., et al. 1987, PhRvD, 35, 785
Akhmedov, E. 1988, PhLB, 213, 64
Akhmedov, E., & Pulido, J. 2003, PhLB, 553, 7
Alexeyev, E., Alexeyeva, L., Krivosheina, I., & Volchenko, V. 1988, PhLB, 205, 209
Allison, J., Amako, K., Apostolakis, I., et al. 2006, ITNS, 53, 270
Allison, J., Amako, K., Apostolakis, J., et al. 2016, NIMPA, 835, 186
An, F., An, G., An, Q., et al. 2016, JPhG, 43, 030401
An, F. P., Balantekin, A. B., Band, H. R., et al. 2017, ChPhC, 41, 013002
Anderson, M., Andringa, S., Asahi, S., et al. 2019, PhRvD, 99, 012012
Ankowski, A. M., Benhar, O., Mori, T., Yamaguchi, R., & Sakuda, M. 2012, PhRvL, 108, 052505
Antonioli, P., Ghetti, C., Korolkova, E., Kudryavtsev, V., & Sartorelli, G. 1997, APh, 7, 357
Argüelles, C. A., Diaz, A., Kheirandish, A., et al. 2019, arXiv:1912.09486
Asakura, K., Gando, A., Gando, Y., et al. 2015a, in AIP Conf. Proc. 1666, 26th Int. Conf. on Neutrino Physics and Astrophysics, ed. E. Kearns & G. Feldman (Melville, NY: AIP), 170003
Asakura, K., Gando, A., Gando, Y., et al. 2015b, ApJ, 806, 87
Asakura, K., Gando, A., Gando, Y., et al. 2015c, PhRvD, 92, 052006
Athar, M. S., Ahmad, S., & Singh, S. K. 2007, PhRvD, 75, 093003
Bays, K., Iida, T., Abe, K., et al. 2012, PhRvD, 85, 052007
Beda, A. G., Brudanin, V. B., Egorov, V. G., et al. 2013, PPNL, 10, 139
Berger, B. E., Busenitz, J., Classen, T., et al. 2009, JInst, 4, P04017
Berger, C., & Sehgal, L. M. 2007, PhRvD, 76, 113004
Böhlen, T., Cerutti, F., Chin, M., et al. 2014, NDS, 120, 211
Bionta, R. M., Blewitt, G., Bratton, C. B., et al. 1987, PhRvL, 58, 1494
Bodek, A., & Yang, U. K. 2003, in AIP Conf. Proc. 670, Particles and Fields: Tenth Mexican School, ed. U. Cotti et al. (Melville, NY: AIP), 110
Bradford, R., Bodek, A., Budd, H., & Arrington, J. 2006, NuPhS, 159, 127
Bratton, C. B., Casper, D., Ciocio, A., et al. 1988, PhRvD, 37, 3361
Calabrese, R., Fiorillo, D. F. G., Miele, G., Morisi, S., & Palazzo, A. 2021, arXiv:2106.02492
Dasgupta, B., Laha, R., & Ray, A. 2020, PhRvL, 125, 101101
Díaz, J. S., Kostelecký, V. A., & Mewes, M. 2009, PhRvD, 80, 076007
Feldman, G. J., & Cousins, R. D. 1998, PhRvD, 57, 3873
Ferrari, A., Sala, P. R., Fasso, A., & Ranft, J. 2005, FLUKA: A Multi-Particle Transport Code, Technical Report, SLAC-R-773
Gando, A., Gando, Y., Hachiya, T., et al. 2016, PhRvL, 117, 082503
Gando, A., Gando, Y., Hanakago, H., et al. 2013, PhRvD, 88, 033001
Gando, A., Gando, Y., Hanakago, H., et al. 2015, PhRvC, 92, 055808
Gando, A., Gando, Y., Ichimura, K., et al. 2011a, NatGe, 4, 647
Gando, A., Gando, Y., Ichimura, K., et al. 2011b, PhRvD, 83, 052002
Gando, A., Gando, Y., Ichimura, K., et al. 2012, ApJ, 745, 193
Gando, Y. 2020, JPhCS, 1468, 012142

Gando, Y., Gando, A., Hachiya, T., et al. 2021, JInst, 16, P08023
Geographical Survey Institute of Japan 1997, Digital Map 50 m Grid (Elevation), unpublished
Glück, M., Reya, E., & Vogt, A. 1998, EPJC, 5, 461
Graczyk, K. M., & Sobczyk, J. T. 2009, PhRvD, 79, 079903
Gran, R., Nieves, J., Sanchez, F., & Vacas, M. J. V. 2013, PhRvD, 88, 113007
Guo, Z., Bathe-Peters, L., Chen, S., et al. 2021, ChPhC, 45, 025001
Hayato, Y. 2009, AcPPB, 40, 2477
Hayato, Y., & Pickering, L. 2021, EPJST, in press
Hirata, K., Kajita, T., Koshiba, M., et al. 1987, PhRvL, 58, 1490
Hirata, K. S., Kajita, T., Koshiba, M., et al. 1988, PhRvD, 38, 448
Honda, M., Athar, M. S., Kajita, T., Kasahara, K., & Midorikawa, S. 2015, PhRvD, 92, 023004
Honda, M., Kajita, T., Kasahara, K., Midorikawa, S., & Sanuki, T. 2007, PhRvD, 75, 043006
Horiuchi, S., Beacom, J. F., & Dwek, E. 2009, PhRvD, 79, 083013
Hostert, M., & Pospelov, M. 2021, PhRvD, 104, 055031
Huber, P. 2011, PhRvC, 84, 024617
Kamei, Y. 2020, JPhCS, 1468, 012241
Kamyshkov, Y., & Kolbe, E. 2003, PhRvD, 67, 076007
Kaplinghat, M., Steigman, G., & Walker, T. P. 2000, PhRvD, 62, 043001
Kim, K., & Cheoun, M.-K. 2009, PhLB, 679, 330
Klop, N., & Ando, S. 2018, PhRvD, 98, 103004
Li, M., Guo, Z., Yeh, M., Wang, Z., & Chen, S. 2016, NIMPA, 830, 303
Lim, C.-S., & Marciano, W. J. 1988, PhRvD, 37, 1368
Malaney, R. A., Meyer, B. S., & Butler, M. N. 1990, ApJ, 352, 767
Mueller, T. A., Lhuillier, D., Fallot, M., et al. 2011, PhRvC, 83, 054615
Nakamura, R., Sambonsugi, H., Shiraishi, K., & Wada, Y. 2020, JPhCS, 1468, 012256
Nakazato, K., Mochida, E., Niino, Y., & Suzuki, H. 2015, ApJ, 804, 75
Nakazato, K., Sumiyoshi, K., Suzuki, H., et al. 2013, ApJS, 205, 2
Nieves, J., Simo, I. R., & Vacas, M. J. V. 2011, PhRvC, 83, 045501
Nowak, J. A. 2009, in AIP Conf. Proc. 1189, Sixth International Workshop on Neutrino-Nucleus Interactions in the Few-GeV Region (NUINT-09) (Melville, NY: AIP), 243
Obara, S., Gando, Y., & Ishidoshiro, K. 2019, PTEP, 2019, 073H01
Ozaki, H., & Shirai, J. 2017, in Proc. of Science 282, Proc. 38th Int. Conf. on High Energy Physics (ICHEP2016) (Trieste: SISSA), 1161
Palomares-Ruiz, S., & Pascoli, S. 2008, PhRvD, 77, 025025
Pena-Garay, C., & Serenelli, A. 2008, arXiv:0811.2424
Punzi, G. 2003, Statistical Problems in Particle Physics, Astrophysics, and Cosmology, Proc. of the PHYSTAT 2003 Conf., 79, https://www.slac.stanford.edu/econf/C030908/
Smirnov, A. Y. 2005, PhST, T121, 57
Steigman, G., Dasgupta, B., & Beacom, J. F. 2012, PhRvD, 86, 023506
Suzuki, A. 2014, EPJC, 74, 3094
Takeuchi, A., & Kawada, N. 2020, JPhCS, 1468, 012155
Wang, S., Xia, D.-M., Zhang, X., Zhou, S., & Chang, Z. 2021, PhRvD, 103, 043010
Zhang, H., Abe, K., Hayato, Y., et al. 2015, APh, 60, 41